Mesoscale eddy characteristics in the interior subtropical southeast Indian Ocean, tracked from the Leeuwin Current system

Huabin Mao[1,4], Ming Feng[1*], Helen E. Phillips[2,3], Shumin Lian[4]

[1] CSIRO Oceans and Atmosphere, Crawley, WA, Australia

[2]IMAS, University of Tasmania, Hobart TAS 7001, Australia.

[3] ARC Centre of Excellence in Climate Extremes, Hobart TAS 7001, Australia.

[4] State Key Laboratory of Tropical Oceanography, South China Sea Institute of Oceanology, Chinese Academy of Sciences, Guangzhou, China

*Corresponding author (ming.feng@csiro.au)

Abstract: Two oppositely rotating mesoscale eddies, originating from the Leeuwin Current, were captured during a research cruise in the interior southeast Indian Ocean in August 2012, a few hundred kilometers off the west coast of Australia. The two eddies had different vertical structures: the anticyclonic eddy had stronger vertical shear above 200m and a less stratified thermocline below the mixed layer, while the cyclonic eddy had a more barotropic structure in the upper 500 m. Compared with the same types of eddies sampled in 2003 close to the Australian coast, the 2012 anticyclonic eddy had a larger radius, deeper isothermal depths, and higher peak velocity; whereas the 2012 cyclonic eddy had a similar structure with the 2003 survey. We use an Argo float and three surface drifters deployed and trapped in the anticyclonic eddy to track its evolution over a 4-month period. The eddy was observed to propagate 1000 km further to the west, indicating that the Leeuwin Current properties of the eddy may be preserved for over 2000 km off the west coast of Australia. The eddy appeared to have experienced radial excursions relative to the eddy center, with periodicity of 4-6 days and 15 days, during their anticlockwise motions. The radial movements of the drifters appeared to be constrained by the radial momentum balance within the eddy. The importance of eddy distortions to ocean primary production in anticyclonic eddies in the southeast Indian Ocean warrants further studies.

Keywords: South Indian Ocean, Leeuwin Current, Mesoscale eddies, Eddy tracking

1. Introduction

Mesoscale eddies are important in transporting heat and water properties in the ocean and play a leading role in the global ocean energy distributions (Qiu and Chen, 2010). Eddies also play an important role in pumping nutrients into the euphotic zone to drive primary production in the ocean (McGillicuddy et al. 2008). The Leeuwin Current in the southeast Indian Ocean possesses stronger mesoscale eddy energy than other mid-latitude eastern boundary current systems (Feng et al. 2005; Zheng et al. 2018). Eddy activities in the Leeuwin Current are important in the heat and momentum balances of the boundary current (Feng et al. 2005; Domingues et al. 2006) and regional biogeochemical processes (Moore et al. 2007; Paterson et al. 2008; Waite et al. 2016).

Anticyclonic eddies from the Leeuwin Current are found to propagate long distances offshore (Morrow et al. 2003), potentially affecting water properties in the interior Indian Ocean. Anticyclonic eddies trap high chlorophyll shelf waters as they are formed by instability of the poleward Leeuwin Current (Rennie et al. 2007). These eddies are found to maintain their high chlorophyll concentration signatures for long periods of time after they propagate into the interior southern Indian Ocean (Feng et al., 2007; Greenwood et al., 2007). Cold-core cyclonic eddies also form through instability of the Leeuwin Current, although they capture less productive offshore waters (Rennie et al. 2007). In the southern Indian Ocean, warm-core anticyclonic eddies tend to be more productive compared to cyclonic eddies (Gaube et al., 2013; Dufois et al., 2014). In addition to the offshore nutrient/biomass transport, high chlorophyll concentrations in warm-core anticyclonic eddies in the southern Indian Ocean have also been attributed to eddy Ekman pumping (Gaube et al., 2013), and wintertime entrainment mixing (Dufois et al., 2014).

Satellite altimeter data are the main tool to identify and define mesoscale eddies in the open ocean (Chelton et al. 2007). Altimeter sea level anomaly (SLA) data has been widely used in tracking mesoscale eddies, and the methods of identifying

75 mesoscale eddies are evolving (Qiu and Chen, 2010; Dong et al., 2011, Faghmous et
76 al. 2017). One of the most commonly used methods is based on the properties of the
77 Okubo–Weiss parameter (Okubo, 1970; Weiss, 1991), which is frequently used to
78 detect eddies from SLA data (Isern-Fontanet et al. 2003; Morrow et al. 2004; Chelton
79 et al. 2007; 2011). Another method can be classified as a hybrid: a physical quantity
80 (SLA) is used to identify eddies, and the streamlines of the flow field are used to define
81 eddy boundaries (Chaigneau et al. 2008). Nencioli et al. (2010) developed an algorithm
82 in which eddy detection is based on velocity derivatives as well as from the SLA field.
83 Oceanic surface drifter trajectories have also been used to identify eddies based on
84 looping segments within a drifter trajectory (Li et al. 2011; Peng et al., 2015a; Peng et
85 al., 2015b). The accuracy of these eddy definitions needs to be evaluated using *in situ*
86 observations (Isern-Fontanet, et al. 2003; Peliz, et al. 2005; Feng et al. 2007; Dickey et
87 al.2008; Nencioli et al. 2008; Paterson, et al. 2008; Kersale, et al. 2013).

88 In August-September 2012, research vessel (R/V) Southern Surveyor sampled an
89 anticyclonic eddy and a cyclonic eddy in the interior subtropical southeast Indian Ocean,
90 with the aim to better characterise the 3-dimensional physical and biogeochemical
91 structure of the Leeuwin Current eddies. These observations provided a unique
92 opportunity to examine the physical dynamics of these eddies which were likely
93 sourced from the Leeuwin Current system. This would allow us to understand the
94 relative roles of the deep nutrient pump due to eddy dynamics, and mixing and nitrogen
95 fixation in maintaining the high chlorophyll concentrations in the anticyclonic eddies,
96 in contrast with the physical processes at work in the cyclonic eddy.

97 In this paper, we examine data from one bio-Argo float and three surface drifters
98 deployed in one anticyclonic (anti-clockwise rotating, warm-core) eddy, and one bio-
99 Argo float in a cyclonic (clockwise rotating, cold-core) eddy. Both eddies were
100 surveyed in the subtropical southeast Indian Ocean during the R/V Southern Surveyor
101 voyage in late 2012. Our focus is determining the physical characteristics of each eddy
102 based on the looping trajectories of the floats and drifters, as well as the shipboard

survey. Section 2 of this paper describes the methods used for eddy detection and tracking. Section 3 shows results from the eddy structure and eddy tracking; in Section 4, we summarize the results, and discuss the comparisons with a Leeuwin Current eddy pair surveyed in 2003 as well as examine an oscillatory feature identified in the anticyclonic eddy. A companion paper will examine the changing biomass properties within the eddies based on the biogeochemical data "Biogeochemical Argo floats reveal the vertical structure of Indian Ocean eddies", Strutton et al., In prep.)

2. Data and Methods

2.1 Data

The primary data used in this study are trajectories from two bio-Argo floats and three surface drifters that were deployed from R.V. Southern Surveyor V04 (11 August – 6 September 2012) in the subtropical southeast Indian Ocean. We named the sea surface drifters S1, S2, and S3, and named the bio-Argo floats A1 and A2 (Table 1). The three drifters and A1 were used to study an anticyclonic eddy, and A2 was used to study a cyclonic eddy. The instruments were trapped in the two eddies for 3-4 months (Figs. 1).

The Argo floats were Teledyne Webb Research APEX floats equipped with SBE41 CTD, Iridium telemetry, Aanderaa Oxygen Optode 3830 and WetLabs FLBBCD-AP2 bio-optical sensors. The floats were programmed to cycle continuously between the surface and 300 dbar, descending to 2000 dbar every 3 days to allow calibration of the salinity sensor. The CTD data was binned into 2 dbar depth.

The surface drifters were provided by the Global Surface Drifter Program (http://www.aoml.noaa.gov/phod/dac/index.php). They were fitted with a holey-sock drogue centered at 15 m depth to measure mixed layer currents and near-surface temperature. Data was transmitted every 6 hours to the Argos satellites and was available on the GTS in near-real time.

129 Shipboard observations included underway acoustic Doppler current profiling
130 (ADCP), and thirty CTD and lowered ADCP (LADCP) profiles to 2000 dbar. The
131 Teledyne RDI 75kHz ADCP measured the ocean currents from 29 m to about 500 m
132 depth in 8 m bins. The CTD unit was a Seabird SBE 911plus CTD. Bottle samples were
133 taken at 12 depths on each station to calibrate the salinity and oxygen sensors, and to
134 measure nutrients. The LADCP is not discussed in this paper because the shipboard
135 ADCP data provided continuous sampling across the eddy and was consistent with the
136 LADCP data at the CTD/LADCP stations. Bad weather during the sampling of the
137 cyclonic eddy resulted in some data gaps in the shipboard ADCP record.

138 Satellite altimeter SLA data from 1 January 2012 to 31 December 2015 were used
139 to track the lifetime of the eddy. We obtained the data from Archiving Validation and
140 Interpretation of Satellite Oceanographic data (AVISO) (ftp://ftp.aviso.altimetry.fr/).
141 Merged sea level anomaly (SLA) data came from two satellite missions,
142 TOPEX/Poseidon and ERS, followed by Jason-1 and Envisat (AVISO, 2006). The
143 mapped altimetry dataset included one map every day with a 0.25° spatial resolution on
144 a Mercator grid (Ducet et al. 2000). The sea level anomalies - which by definition
145 provide the differences of the sea level with respect to a reference mean - may display
146 a much weaker signal than the sea level with respect to the geoid for slowly evolving
147 eddies, because part of the quasi-permanent signal of the eddy is absorbed in the
148 reference mean. The two eddies studied in the manuscript seem to be quite dynamical,
149 so that their signal is not attenuated in the sea level anomalies.

150 World Ocean Atlas 2013 data are obtained from NOAA National Oceanographic
151 Data Center (Boyer et al. 2013).

152 **2.2 Methods**

153 Statistical census of eddies from Lagrangian drifter trajectory data has been
154 conducted in many studies (e.g., Richardson, 1993; Chaigneau and Pizarro, 2005;
155 Shoosmith et al. 2005; Fratantoni and Richardson, 2006; Hamilton, 2007; Berti et al.,

2011; Li et al., 2011; Schroeder et al., 2012; Zu et al., 2012). Similarly, satellite altimeter data has been used extensively to investigate the global characteristics of mesoscale variability (e.g. Ducet et al. 2000; Morrow et al. 2003, 2004; Chelton et al. 2007; Gaube et al. 2013). Here we focus on two methods to track the eddies in which our instruments were trapped. The first method is based on the drifter and Argo trajectory data, following Li et al. (2011). The second uses satellite SLA data following Nencioli et al. (2010).

Li et al. (2011) developed a method that uses discrete loops in the trajectories of surface drifters to determine the changing position and radius of eddies. When a loop is a closed and continuous curve, with its starting point overlapped by its ending point, an eddy is identified. Following their method, we identify the eddy center as follows: 1) find overlapping points along surface drifter trajectories; 2) quality-control the overlapping points to eliminate false points and avoid losing internal overlapping points; 3) determine the polarity of loops; 4) cluster loop trajectories into individual eddies (Fig. 3). The loop center is estimated by geometrically averaging all the sample points along the looping trajectory.

We compared three ways to define the loop (eddy) radius R from the trajectory data: 1) R is the mean distance between all loop points to the loop center (Li et al., 2011; Zheng et al., 2015); 2) R is estimated from the mean looping period (T) and mean swirl speed (V_s) using the relation $R = Vs * T / 2\pi$ (Shoosmith et al., 2005); 3) $R = (ab)^{1/2}$, where a is the minimum distance between loop points and the loop center, b is the maximum distance between loop points and the center (Hamilton et al. 1999).

We also used satellite SLA data to track the eddies followed by the instruments. The algorithm is based exclusively on the geometry of geostrophic velocities determined from satellite SLA (Nencioli et al. 2010). The track of a given eddy at time step t is updated by searching for eddy centers of the same type (e.g. anticyclonic) at time t+1 within a searching area of 50 × 50 km centered around the eddy location at

183 time t. Eddy boundaries were defined as the outermost closed streamline around the
184 eddy center. From the altimeter data, the eddy radius is simply the mean distance from
185 the eddy center to the eddy boundary.

186 For the anticyclonic eddy, we average the eddy centers determined from the 3
187 drifters and the altimeter data and then smooth in time to define the eddy centers that
188 are used to reference the various datasets. For the cyclonic eddy, the eddy centres are
189 only available from the altimeter data. The tangential velocity of the eddies were
190 calculated as a function of distance from the identified eddy centers. The shipboard
191 ADCP velocities at 29m were projected to the tangential direction relative to the eddy
192 center on the day of the ADCP transect across each eddy. The radius was determined
193 using the distance from the center to where the ADCP tangential velocity reached a
194 maximum value. The drifter velocities were projected to the tangential direction relative
195 to the 6-hourly moving eddy center.

196 We calculate the power spectrum of the drifter positions relative to the eddy centre
197 using the method of Papadakis and Lawrence (1993), which is available in the Matlab
198 function rednoise.m. We calculated the red noise spectrum over 100 realizations.

199 Mixed layer depth (MLD) was defined as the depth at which there was a $0.125\,\sigma_\theta$
200 increment from the density at 10 m depth in individual CTD profiles from the shipboard
201 and bio-Argo data.

202

203 **3. Results**

204 **3.1 Eddy structures from shipboard observations**

205 The two mesoscale eddies sampled during the August 2012 cruise period were an
206 anticyclonic warm-core eddy located at 105°E, 26.5°S, and a cyclonic cold-core eddy
207 located at 109.5°E, 32.6°S (Fig. 1). The two eddies were identified by their sea level

208 anomaly signatures and the cruise track crossed the centers of both eddies. From the
209 shipboard ADCP current measurements, the eddy centers were identified as the
210 locations of minimum velocities along the cruise track. The tangential velocities of the
211 eddies increased approximately linearly with distance from the center before reaching
212 maximum values at about 80 km (anticyclonic) and 50 km (cyclonic).

213 The anticyclonic eddy had a bowl shape with isotherms depressed by around 100
214 m at the centre of the eddy relative to the edges (Fig. 2a). The core of the eddy was
215 warm and fresh, with isohalines displaying the same bowl shape. The low salinity
216 signature (~35 psu) in the surface layer is likely derived from its Leeuwin Current
217 source (Feng et al. 2007). High salinity subtropical water (STW) forms a subsurface
218 salinity maximum at 100-300 m depth above a low salinity layer below 400 m depth.
219 The eddy structure extended to the 2000 m limit of the CTD observations.

220 Within the cyclonic eddy, the isotherms displayed a significant dome shape only
221 below 300m (Fig. 2d, e), which is consistent with weak vertical shear in the eddy (Fig.
222 2f). There was strong stratification and weak current shear (high Richardson number)
223 below the mixed layer of the cyclonic eddy and the mixing across the base of the mixed
224 layer may not be strong (not shown). Although vertical shear was weak in the cyclonic
225 eddy, the rotational velocities were as strong as those encountered in the surface of the
226 high shear anticyclonic eddy. High salinity subtropical water in the mixed layer of the
227 cyclonic eddy capped the low salinity Antarctic Intermediate Water in the subsurface.
228 (Fig.2e).

229 We investigated the likely Leeuwin Current origin of the warm core eddy by
230 comparing its T-S structure with profiles from the World Ocean Atlas. Figure 3
231 compares the T-S profile from shipboard data at the centre of the anticyclonic eddy,
232 and a WOA profile at the location where the eddy was first seen in the altimeter record
233 (Section 3.2). We also show the profile at the centre of the cyclonic eddy for contrast.
234 It is clear from the features in T-S profiles that the watermass properties of the

anticyclonic eddy are consistent with it forming within the Leeuwin Current. The warmer and fresher signature of the anticyclonic eddy mixed layer salinity in the CTD observations relative to WOA may be related to the warming and freshening of the Indonesian Throughflow and the Leeuwin Current prior to the survey period associated with the Pacific climate variability (Feng et al. 2015a, b).

In summary, the anticyclonic eddy was larger and stronger than the cyclonic eddy in the surface layer. The two eddies had different vertical structures; the anticyclonic eddy had stronger vertical shear above 200 m and a less stratified thermocline below the mixed layer, while the cyclonic eddy had a more barotropic structure in the upper 500 m and the isothermal doming did not reach the surface layer.

3.2 Eddy tracking

We follow the observed anticyclonic and cyclonic eddy using sea level anomaly, sea surface temperature and surface chlorophyll. Figure 4 shows monthly maps of these fields, from September 2012 to February 2013 while the instruments were within the eddies. The tracks of drifters and Argo floats during each month are overlaid, clearly showing the floats stayed within the eddies. Examining the SLA data prior to the voyage, we saw that the anticyclonic eddy spun off the Leeuwin Current in May 2012 (Fig. 5), whereas the cyclonic eddy developed away from the coast in July 2012. The anticyclonic eddy could be tracked from 28 April 2012 to 19 February 2013, with its radius ranging from 34 km to 180 km with an average of 100 km, and its amplitude ranging from 36 to 49 cm. The cyclonic eddy could be tracked from 16 July 2012 to 25 July 2014. Its radius ranged from 36 km to 106 km with an average of 66 km. Both eddies moved westward. The anticyclonic eddy moved at an average of 13.7 km/day and the cyclonic eddy at 2.7 km/day, based on the speed of translation of the eddy centers.

We next examine the eddy characteristics determined directly from the drifter and float trajectories. All instruments experienced looping trajectories and we identified

between 6 and 17 closed loops within each trajectory (Figure 6, Table 1). The loops within the anticyclonic eddy were large and clear over the 1000 km distance it travelled during the 4 month period. The loops from the Argo float in the cyclonic eddy were large and clear at the start of the record but the radius reduced dramatically in the middle of the record to the point where the looping appeared to be more like inertial circles. We examined the position of the Argo float relative to the eddy, stepping through the altimeter record in increments of 14 days (Figure 7). It is clear that the float stayed within the core of the eddy over its lifetime. The shrinking of the loops suggests that there was convergent flow within the eddy that caused the float to be drawn towards the centre of the eddy, dramatically shrinking the loop radii toward the end of the record.

3.3 Rotation of the anticyclonic eddy

The tangential velocities of the anticyclonic eddy derived from drifter tracks (Section 2.2) are compared with ADCP measured velocities in Figure 8, which shows the relationship between the near surface (29 m) tangential velocity and distance to eddy center in the anticyclonic eddy. The black line is the second order polynomial fit of the zonal (tangential) velocity from the meridional ADCP section across the anticyclonic eddy. Maximum velocities of about 50 cm/s were found at a radius of 90 km, while velocities at larger distances from the center tended to decrease. Linear fits to the drifter velocities were close to the polynomial fit to the ADCP data out to about 60 km. Beyond 60 km, the polynomial fit to the ADCP data showed a further increase in velocity to a maximum at a radius of about 90 km. At 90 km, the relative vorticity was about 1.1% of the Coriolis parameter, f, suggesting that the edges of this eddy are in geostrophic balance. Thus, the geostrophic relationship is suitable to be used to determine the tangential velocity at the eddy edges from altimetry measurements.

3.3 Distortions of the anticyclonic eddy

When tracked relative to the center of the anticyclonic eddy, all 3 drifters followed

close to circular paths around the eddy centers (Fig. 9 a-c), however, the time series of the distance of each drifter from the eddy center contained periodic fluctuations (Fig. 9 d). In the power spectrum calculated from the distance between each drifter and the eddy center, there was a significant peak at 0.23 cpd, corresponding to a 4.4 day period for S1, and a 0.25 cpd peak, or 4.0 days period for S3. The S2 spectrum had two peaks at 0.16 cpd and 0.22 cpd, or 6.4 days and 4.5 days period, respectively (Fig. 9). Thus, all of the 3 drifters showed short period oscillations of 4-6 days relative to the anticyclonic eddy center.

To quantify the relationship between horizontal distance and the vertical movement of isopycnals at the center of the anticyclonic eddy, we adopted a universal structure in normalized stretched coordinates, following Zhang et al. (2013). Horizontally, the isopycnal depth anomaly is described by a function of the normalized radial distance from the eddy center $R(r_n) = (1 - r_n^2/2) \cdot \exp(-r_n^2/2)$, where r_n is the radial distance from the eddy center. We define H_0 as the depth of the 25.5 kg/m^3 isopycnal at the eddy center, H_{rn} means the depth of the 25.5 kg/m^3 isopycnal at the radial distance r_n. Therefore, the standardized isopycnal depth anomaly at the eddy center is, $H_0 = H_{rn} / R(r_n) = H_{rn} / ((1 - r_n^2/2) \cdot \exp(-r_n^2/2))$. The variations of mixed layer depth derived from the A1 Argo data agreed well with variations in isopycnal depths, and when the Argo float moved away from the eddy center, both the mixed layer depth and isopycnal depth became shallower (Fig. 10). There appeared to be a periodicity of ~15 days of the position of the A1 Argo float relative to the anticyclonic eddy center (not shown). It is not surprising that the periodicity of the Argo float is quite different to that of the drifters given that it profiles to 300 dbar continuously whereas the drifters stay at the sea surface.

4. Summary and Discussion

313 In this study, we used satellite data, sea surface drifters, Argo and shipboard data
314 to track two mesoscale eddies and their evolving characteristics in the southeast Indian
315 Ocean during 2012. The anticyclonic eddy formed in the Leeuwin Current off the west
316 coast of Australia; whereas the cyclonic eddy was first detected offshore of the Leeuwin
317 Current. Three surface drifters and one Argo float tracked the anticyclonic eddy for four
318 months, and one Argo float tracked the cyclonic eddy for the same period. The
319 anticyclonic eddy had larger amplitude and faster tangential velocity than the cyclonic
320 eddy in the surface layer. The two eddies had different vertical structures: anticyclonic
321 eddy had stronger vertical shear above 200m and a less stratified thermocline below the
322 mixed layer, while the cyclonic eddy had a more barotropic structure in the upper 500
323 m. Compared with the same types of eddies sampled in 2003, as described by Feng et
324 al. (2007), the anticyclonic eddy was farther away from the coast, had a larger radius,
325 deeper isothermal depths, and higher peak velocity; whereas the cyclonic eddy had a
326 similar structure to that sampled in 2003 (Table 2). The peak velocity of the anticyclonic
327 eddy decreased from 73 cm s^{-1} at 30 m to about 40 cm s^{-1} at 300 m, while the peak
328 velocity of the cyclonic eddy was almost constant with depth at around 60-70 cm s^{-1} in
329 the upper 400 m. The radius of the anticyclonic eddy was about 80 km and the radius
330 of the cyclonic eddy was about 50 km.

331 Eddy characteristics derived from drifters are compared with those from satellite
332 and shipboard data. Table 3 shows the mean period of the drifter track loops, and mean
333 radii of the loops estimated using the 3 methods for the anticyclonic eddy described in
334 Section 2.2. The mean periods determined for the 3 drifters were similar, while the
335 mean radius varied by up to a factor of 2 between drifters, and between methods,
336 especially for S1 and S3. The mean radius and range of radii, derived from satellite data
337 (Nencioli et al. 2010), are also shown in Table 3. The satellite-derived radius was 2-5
338 times larger than that observed by the drifters. The mean radius estimated from
339 shipboard data (80 km, Fig.3) was also two times larger than observed by the drifters.
340 This suggests that the drifters were following interior streamlines of the eddy and that

341 the radii of closed-loop trajectories were not indicative of the size of the eddy.

342 Based on three drifters and one Argo float, the anticyclonic eddy appeared to have
343 experienced 4-6 day and 15-day oscillations of the eddy. The oscillatory nature of the
344 drifter movements denotes strong alternating divergent and convergent motions in the
345 interior of the eddy, which warrants further study. Earlier studies noticed that eddy
346 pumping leads to rich plankton within eddies (Jyothibabu et al. 2015; Weller et al. 2013).
347 The oscillatory feature of eddy may suggest upwelling and downwelling motion within
348 the eddy, providing new insight into the vertical exchanges in the eddy, which may
349 induce mixing and bring nutrients up toward the sea surface.

350 The physical description of the present study will aid the interpretation of the
351 biogeochemical processes in the two eddies using shipboard survey and bio-Argo data
352 in future studies. The contrast of the two types of eddy structures are consistent with
353 the census of eddies based on satellite altimeter data in the southern Indian Ocean
354 (Gaube et al. 2013; Dufois et al. 2014), with the anticyclonic eddy being more dynamic
355 and potentially more prone for vertical nutrient fluxes whereas the cyclonic eddy having
356 a weaker upwelling and vertical mixing in the near-surface layer. The oscillatory feature
357 of the anticyclonic eddy may also contribute to the nutrient fluxes, which is explained
358 by the momentum balance within the eddy in the following section.

359

360 **Momentum balance of the anticyclonic eddy**

361 Following Zhang et al. (2015), the standardized radial distance (γ) of a given point
362 inside an eddy relative to the eddy center is defined as $\gamma = \frac{A-a}{A}$, where A is the
363 amplitude of the eddy and a is the SLA difference between the point and the eddy edge.
364 The eddy edge was determined by the maximum tangential geostrophic velocity. The
365 geostrophic current velocities from altimeter SLA data were used to derive the relative

366 vorticity within the eddy. The area-averaged Rossby number ε of the eddy is given by,

367 $\varepsilon = \frac{\left|\overline{\zeta_g}\right|}{f}$, where $\left|\overline{\zeta_g}\right|$ is the absolute area-averaged geostrophic vorticity within the

368 eddy edge and f is the Coriolis parameter (Zhang et al., 2015).

369 The momentum balance equation is

370 $$-g\frac{\partial h}{\partial r} + fv + \frac{v^2}{r} = 0 \qquad (1)$$

371 where h is the SLA, r the radial distance outward from the eddy center, v the tangential
372 velocity, and g the gravitational acceleration. Assuming that the rotational velocity is
373 the sum of geostrophic and ageostrophic currents ($v = v_g + v_{ag}$) and sea level slope is
374 balanced by Coriolis acceleration due to geostrophic current, the above equation can be
375 rewritten as

376 $$v_{ag}^2 + \left(2v_g + rf\right)v_{ag} + v_g^2 = 0 \qquad (2)$$

377 The solution of v_{ag} in this equation is possible if $-\frac{v_g}{r} \le 0.25f$, i.e., $\varepsilon \le 0.25$. That

378 is to say, a water parcel can be stable if the Rossby number $\varepsilon \le 0.25$, otherwise it is
379 unstable because of the imbalance of radial momentum. When $\varepsilon < 0.25$, , the sum of
380 pressure gradient, Coriolis, and centrifugal forces is inward and a parcel tends to move
381 toward the eddy center. When $\varepsilon > 0.25$, the balance of forces is outward, driving a parcel
382 toward the eddy edge until a new balance is set up.

383 Figure 11a shows the time series of distance from the anticyclonic eddy center.
384 The black line is the eddy radius from SLA, and the colored lines are the distance from
385 the eddy center of the three drifters. After 25 Sep. 2012, the eddy became stabilized and
386 the floats were trapped within about 60 km from the eddy center. The eddy radius
387 increased from 60km to 120km during 25 September to 30 December, denoting the
388 decay phase of the eddy.

389 The drifters in the anticyclonic eddy experienced large radial excursions during
390 the 18-30 September period, with radial oscillations of about 20-60 km and periodicity
391 of about 5 days. We have chosen three time slices, T1 on 30 Sep. 2012, T2 on 10 Oct.
392 2012, and T3 on 20 Oct. 2012, to analyze the relationship between the local Rossby
393 number and the radial movement of the drifters.

394 Overall, the local Rossby numbers decreased with standardized radial distance, γ:
395 at T1 it decreased from 0.33 at the eddy center to 0.06 at the eddy edge; at T2 it
396 decreased from 0.36 to 0.08; at T3 it decreased from 0.35 to 0.14. At T1 (Fig. 11b), the
397 local Rossby number values at the three drifter locations were mostly under 0.25,
398 indicating that all the drifters were forced by surface convergence to move inward
399 toward the eddy center, as indicated in Figure 11a. At T2 (Fig. 11c), the Rossby number
400 values of S1 and S3 within the inner area $\gamma \leq 0.3$ were above 0.25, indicating that water
401 parcels in this inner area were forced to move outward; the Rossby number values of
402 S2 within the area $\gamma \geq 0.5$ were under 0.25, indicating that the parcels in this inner area
403 were forced to move inward. At T3 (Fig. 11d), the Rossby number values of most points
404 within the eddy were above 0.25, indicating that the parcels in the eddy were forced to
405 move outward.

406 Overall, the oscillatory feature of the anticyclonic eddy suggests a dynamic
407 distortion of the eddy, alternating between convergence and divergence of volume at
408 the eddy centre, which may be important for biogeochemical processes within the eddy.
409 A more detailed evaluation of the relationship between the dynamics of the oscillatory
410 feature and the variability in biogeochemical properties of the eddy needs to be
411 undertaken to better understand their roles in vertical nutrient fluxes in the anticyclonic
412 eddies in the subtropical oceans. Future work is needed to address the question of
413 whether the productivity of warm core Leeuwin Current eddies gradually decays from
414 the level present at formation of the eddy, or whether processes such as dynamic
415 distortion can stimulate productivity through vertical nutrient fluxes to sustain
416 phytoplankton biomass.

Acknowledgements

We greatly appreciate the efforts of the NOAA global drifter program in collecting and distributing surface drifter data, and the Argo Program for delivering profiling float data. Officers, crew and science party of R.V. Southern Surveyor V04 2012 are thanked for the in situ data. This study was also supported by the National Key R&D Plan of China (No. 2017YFC0305804), and the Australian Research Council (DP130102088). This research is also supported by the CAS/SAFEA International Partnership Program for Creative Research Teams. HP acknowledges support from the Australian Government's National Environment Science Program Earth Systems Climate Change Hub. There is no competing interest among the authors. We thank the editors and two anonymous reviewers for constructive comments of an earlier manuscript.

430 **Reference**

431 Berti, S., F. A. Dos Santos, G.Lacorata, and A. Vulpiani, 2011. Lagrangian drifter dispersion in the
432 southwestern Atlantic Ocean. *J. Phys. Oceanogr.*, *41*, 1659–1672.

433 Boebel, O., J. Lutjeharms, C. Schmid, W. Zenk, T. Rossby, and C. Barron, 2003. The Cape Cauldron:
434 A regime of turbulent inter-ocean exchange. *Deep-Sea Res. II*, *50*, 57–86.

435 Boyer, T.P., J. I. Antonov, O. K. Baranova, C. Coleman, H. E. Garcia, A. Grodsky, D. R.
436 Johnson, R. A. Locarnini, A. V. Mishonov, T.D. O'Brien, C.R. Paver, J.R. Reagan, D.
437 Seidov, I. V. Smolyar, and M. M. Zweng, 2013: World Ocean Database 2013, NOAA
438 Atlas NESDIS 72, S. Levitus, Ed., A. Mishonov, Technical Ed.; Silver Spring, MD, 209
439 pp., http://doi.org/10.7289/V5NZ85MT

440 Chaigneau, A. and O. Pizarro, 2005. Eddy characteristics in the eastern South Pacific. *J. Geophys.*
441 *Res.*,*110* (C6).

442 Chaigneau, A., A. Gizolme, and C. Grados, 2008. Mesoscale eddies off Peru in altimeter records:
443 Identification algorithms and eddy spatio-temporal patterns. *Prog. Oceanogr.*, *79* (2–4), 106–
444 119.

445 Chelton, D. B., M. G. Schlax, R. M. Samelson, and R. A. de Szoeke, 2007. Global observations of
446 large oceanic eddies. *Geophys. Res. Lett.*, *34*, L15606, doi:10.1029/2007GL030812.

447 Chelton, D. B., M. G. Schlax, and R. M. Samelson, 2011. Global observations of nonlinear
448 mesoscale eddies. *Prog. Oceanogr.*, *91* (2), 167–216.

449 Dickey, T.D., F.Nencioli, V.S.Kuwahara, C.L.Leonard, W.Black, R.R.Bidigare, Y.M.Rii,and Q.
450 Zhang, 2008. Physical and bio-optical observations of oceanic cyclones west off the island of
451 Hawai'i. *Deep-Sea Res. II*, *55*, 1195 – 1217.

452 Domingues, C.M., Wijffels, S.E., Maltrud, M.E., Church, J.A. and Tomczak, M., 2006. Role of
453 eddies in cooling the Leeuwin Current. *Geophysical research letters*, *33*(5).

454 Dong, C., Y. Liu, R. Lumpkin, M. Lankhorst, D. Chen, J. C. McWillianms, and Y. Guan, 2011. A
455 Scheme to Identify Loops from Trajectories of Oceanic Surface Drifters: An Application in the
456 Kuroshio Extension Region. *J. Atmos. Oceanic Technol.*, *28*(9), 1167-1176.

457 Ducet, N., P.-Y. Le Traon, and G. Reverdin, 2000. Global high-resolution mapping of ocean
458 circulation from Topex/Poseidon and ERS-1 and -2. *J. Geophys. Res.*, *105*, 19477–19498.

459 Dufois, F., N. J. Hardman-Mountford, J. Greenwood, A. J. Richardson, M. Feng, S. Herbette, and

460 R. Matear, 2014. Impact of eddies on surface chlorophyll in the South Indian Ocean. *J.*
461 *Geophys. Res.*, *119* (11), 8061-8077.

462 Faghmous, J. H., I. Frenger, Y. Yao, R. Warmka, A. Lindell, and V. Kumar (2015), A daily
463 global mesoscale ocean eddy dataset from satellite altimetry, *Scientific data*, *2*.

464 Fang, F. and R. Morrow, 2003. Evolution, movement and decay of warm-core Leeuwin Current
465 eddies. *Deep-Sea Res. II*, *50*, 2245 - 2262.

466 Feng, M., S. Wijffels, S. Godfrey and G. Meyers, 2005: Do eddies play a role in the momentum
467 balance of the Leeuwin Current? *Journal of Physical Oceanography*, 35(6), 964-975

468 Feng, M., L. J. Majewski, C. B. Fandry, and A. M. Waite, 2007. Characteristics of two counter-
469 rotating eddies in the Leeuwin Current system off the Western Australian coast. *Deep-Sea Res.*
470 *II*, *54* (8-10), 961-980.

471 Feng, M., H. H. Hendon, S.-P. Xie, A. G. Marshall, A. Schiller, Y. Kosaka, N. Caputi, and A.
472 Pearce 2015a, Decadal increase in Ningaloo Niño since the late 1990s, Geophys. Res.
473 Lett., **42**, 104-112, doi:10.1002/2014GL062509.

474 Feng, M., J. Benthuysen, N. Zhang, and D. Slawinski 2015b. Freshening anomalies in the
475 Indonesian throughflow and impacts on the Leeuwin Current during 2010–2011, Geophys.
476 Res. Lett., **42**, 8555-8562, doi:10.1002/2015GL065848

477 Fratantoni, D. M. and P. L. Richardson, 2006. The evolution and demise of North Brazil Current
478 rings. *J. Phys. Oceanogr.*, *36* (7), 1241-1264.

479 Gaube, P., D. B. Chelton, P. G. Strutton, and M. J. Behrenfeld, 2013. Satellite observations of
480 chlorophyll, phytoplankton biomass, and Ekman pumping in nonlinear mesoscale eddies. *J.*
481 *Geophys. Res.*, *118*(12): 6349-6370.

482 Greenwood, J. E., M. Feng, and A. M. Waite, 2007. A one-dimensional simulation of biological
483 production in two contrasting mesoscale eddies in the southeastern Indian Ocean. *Deep-Sea*
484 *Res. II*, *54* (8-10): 1029-1044.

485 Hamilton, P., G. S. Fargion, and D. C. Biggs, 1999. Loop Current eddy paths in the western Gulf of
486 Mexico. *J. Phys. Oceanogr.*, *29* (6), 1180-1207.

487 Hamilton, P., 2007. Eddy statistics from Lagrangian drifters and hydrography for the northern Gulf
488 of Mexico slope. *J. Geophys. Res.*,*112* (C9), 1-16.

489 Isern-Fontanet, J., E. Garcia-Ladona, and J. Font, 2003. Identification of marine eddies from

490 altimetric maps. *J. Atmos. Oceanic. Technol.*, *20*, 772–778.

491 Jia, F., L. Wu, and B. Qiu, 2011. Seasonal modulation of eddy kinetic energy and its formation
492 mechanism in the southeast Indian Ocean. *J. Phys. Oceanogr.*, *41* (4), 657-665.

493 Jyothibabu, R., P. N.Vinayachandran, N. V. Madhu, R. S. Robin, C. Karnan, L. Jagadeesan and A.
494 Anjusha., 2015. Phytoplankton size structure in the southern Bay of Bengal modified by the
495 Summer Monsoon Current and associated eddies: Implications on the vertical biogenic flux. *J.*
496 *Marine Syst.*, *143*, 98-119.

497 Kersale, M., A. A. Petrenko, A. M. Doglioli, I. Dekeyser and F. Nencioli, 2013. Physical
498 characteristics and dynamics of the coastal Latex09 Eddy derived from in situ data and
499 numerical modeling. *J. Geophys. Res.*, *118*(1), 399-409.

500 Lankhorst, M., 2006. A self-contained identification scheme for eddies in drifter and float
501 trajectories. *J.Atmos. Oceanic. Technol.*, *23*, 1583–1592.

502 Lankhorst, M. and W. Zenk, 2006. Lagrangian observations of the mid-depth and deep velocity
503 fields of the northeastern Atlantic Ocean. *J. Phys. Oceanogr.*, *36*, 43–63.

504 Li, J. X., R. Zhang, and B. G. Jin, 2011. Eddy characteristics in the northern South China Sea as
505 inferred from Lagrangian drifter data. *Ocean Sci.*, *7* (5), 661-669.

506 McGillicuddy, D. J., J. R. Ledwell, and L. A. Anderson, 2008. Response to comment on "Eddy/wind
507 interactions stimulate extraordinary mid-ocean plankton blooms". *Science*, *320*, 5875.

508 McWilliams, J. C., E. D. Brown, and H. L.Bryden,1983. The local dynamics of eddies in the western
509 North Atlantic, in Eddies in Marine Science, edited by A. R. Robinson, pp. 92 - 113, Springer,
510 Berlin.

511 McWilliams, J. C., L. P. Graves, and M. T. Montgomery, 2003. A formal theory for vortex Rossby
512 waves and vortex evolution, *Geophys. Astrophys. Fluid Dyn.*, *97*, 275 - 309.

513 Moore, T. S., R. J. Matear, J. Marra and L. Clementson, 2007. Phytoplankton variability off the
514 Western Australian Coast: Mesoscale eddies and their role in cross-shelf exchange. *Deep-Sea*
515 *Res. II,54* (8-10), 943-960.

516 Morrow, R., F. X. Fang and M. Fieux, 2003. Anatomy of three warm-core Leeuwin Current eddies.
517 *Deep-Sea Res. II*, *50* (12-13), 2229-2243.

518 Morrow, R., F. Birol, D. Griffin, and J. Sudre, 2004. Divergent pathways of cyclonic and anti-
519 cyclonic ocean eddies. *Geophys. Res. Lett.*, *31*, L24311, doi:10.1029/2004GL020974.

520 Nencioli, F., V. S. Kuwahara, T. D. Dickey, Y. M. Rii, and R. R. Bidigare, 2008. Physical dynamics
521 and biological implications of a mesoscale eddy in the lee of Hawai'i: Cyclone Opal
522 observations during E-FLUXIII. *Deep-Sea Res. II*, 55 (10–13), 1252–1274.

523 Nencioli, F., C. M. Dong, T. Dickey, L. Washburn and J. C. McWilliams, 2010. A vector geometry-
524 based eddy detection algorithm and its application to a high-resolution numerical model
525 product and high-frequency radar surface velocities in the Southern California Bight. *J.Atmos.*
526 *Oceanic Technol.*, *27* (3), 564-579.

527 Okubo, A., 1970. Horizontal dispersion of floatable particles in vicinity of velocity singularities
528 such as convergences. *Deep-Sea Res.*, *17*, 445–454.

529 Papadakis, I. E. and A. Lawrence, 1993. Improved methods for power spectrum modeling of red
530 noise. *Mon. Not. R. Astron. Soc.*, *261*(3), 612-624.

531 Paterson, H. L., M. Feng, A. M. Waite, D. Gomis, L. E Beckley, D. Holliday, and P. A. Thompson,
532 2008. Physical and chemical signatures of a developing anticyclonic eddy in the Leeuwin
533 Current, eastern Indian Ocean. *J. Geophys. Res.*, *113*(C7), 827-830.

534 Peliz, A., J. Dubert, A. M. P. Santos, P. B. Oliveira, and B. L. Cann, 2005. Winter upper ocean
535 circulation in the Western Iberian Basin - Fronts, Eddies and Poleward Flows: an overview.
536 *Deep-Sea Res. I*, *52*(4), 621-646.

537 Peng, S. Q., Y. K. Qian, R. Lumpkin, Y. Du, D. X. Wang, and P. Li. Characteristics of the Near-
538 Surface Currents in the Indian Ocean as Deduced from Satellite-Tracked Surface Drifters. Part
539 I: Pseudo-Eulerian Statistics. *J. Phys. Oceanogr.*, *45*, 441–458.

540 Peng, S. Q., Y. K. Qian, R. Lumpkin, P. Li, D. X. Wang, and Y. Du. Characteristics of the Near-
541 Surface Currents in the Indian Ocean as Deduced from Satellite-Tracked Surface Drifters. Part
542 II: Lagrangian Statistics. *J. Phys. Oceanogr.*, *45*, 459–477.

543 Pingree, R. D., and B. Le Cann, 1992. Three anti-cyclonic Slope Water Oceanic eDDIES
544 (SWODDIES) in the Southern Bay of Biscay. *Deep-Sea Res. I*, *39*, 1147– 1175.

545 Qiu, B. and S. M. Chen, 2010. Interannual variability of the North Pacific Subtropical
546 Countercurrent and its associated mesoscale eddy field. *J. Phys. Oceanogr.*, *40* (1), 213-225.

547 Rennie, S. J., C. P. Pattiatatchi, R D. McCauley, 2007. Eddy formation through the interaction
548 between the Leeuwin Current, Leeuwin Undercurrent and topography. Deep-Sea Research II,
549 54, 789–796. doi:10.1016/j.dsr2.2007.02.005.

550 Richardson, P. L., 1993. A census of eddies observed in North Atlantic SOFAR float data. *Prog.*

551 *Oceanogr.*, *31*, 1–50.

552 Schmid, C., R. L. Molinari, R. Sabina, et al, 2007. The real-time data management system for Argo
553 profiling float observations. *J.Atmos. OceanicTechnol.*,*24* (9): 1608-1628.

554 Schroeder, K., J. Chiggiato, A. C.Haza, et al., 2012. Targeted Lagrangian sampling of submesoscale
555 dispersion at a coastal frontal zone. *Geophys. Res. Lett.*, *39*, L11608,
556 doi:10.1029/2012gl051879.

557 Shoosmith, D. R., P. L. Richardson, A. S. Bower, and H. T. Rossby, 2005. Discrete eddies in the
558 northern North Atlantic as observed by looping RAFOS floats. *Deep-Sea Res. I*, *52* (3-4), 627-
559 650.

560 Smith, R.L.,Huyer, A., Godfrey, J.S. and Church, J., 1991. The Leeuwin Current off Western
561 Australia, 1986-1987. *J. Phys. Oceanogr.*, 21, 323-345.

562 van Aken, H. M., 2002. Surface currents in the Bay of Biscay as observed with drifters between
563 1995 and 1999. *Deep-Sea Res. I*, *49*, 1071 - 1086.

564 Waite, A. M., L. E. Beckley, L. Guidi, J. Landrum, D. Holliday, J. Montoya, H. Paterson, M.
565 Feng, P. A. Thompson, and E. J. Raes (2016), Cross-shelf transport, oxygen depletion and
566 nitrate release within a forming mesoscale eddy in the eastern Indian Ocean, *Limnol.*
567 *Oceanogr.*, 61, 103-121, DOI: 10.1002/lno.10218.

568 Weiss, J., 1991. The dynamics of enstrophy transfer in 2-dimensional hydrodynamics. *Physica D*,
569 *48 (2–3)*, 273–294.

570 Weller, D. I., C. S.Law, A. Marriner, S. D.Nodder, F. H.Chang, J. A.Stephens, S. W. Wilhelm, P.
571 W. Boyd, and P. J. H. Sutton, 2013. Temporal variation of dissolved methane in a subtropical
572 mesoscale eddy during a phytoplankton bloom in the southwest Pacific Ocean. *Prog.*
573 *Oceanogr.*,*116*, 193-206.

574 Zhang, Z. W., Y. Li, and J. W. Tian, 2013. A modified method to estimate eddy diffusivity in the
575 North Pacific using altimeter eddy statistics. *Chinese Journal of Oceanology and Limnology*,
576 *31*(4), 925-933.

577 Zheng, S., Y. Du, J. Li, and X. Cheng, 2015. Eddy characteristics in the south Indian Ocean as
578 inferred from surface drifters. *Ocean Sci.*, *11*(3), 361-371.

579 Zheng, S., Feng, M., Du, Y., Meng, X. and Yu, W., 2018. Interannual Variability of
580 Eddy Kinetic Energy in the Subtropical Southeast Indian Ocean Associated With
581 the El Niño-South Oscillation.Journal of Geophysical Research: Oceans, 123,

582 1048-1061.

583 Zu, T. T., J. Chen, and D. X. Wang, 2012. Detection of the Cyclonic Eddy in the southwest of the
584 South China Sea: from remote sensing data and drifter buoys. *Adv. Intel Soft. Compu.*, *142*,
585 153 - 159.

586

587

588 Table 1. Deployment information for the three drifters and two Argo floats, and the
589 numbers of loops observed.

WMO ID	Instrument	Eddy	Start Position (lat, lon)	First obs.	Last obs.	loops
109245	S1	Anticyclonic	27.00°S, 105.00°E	22 Sep 2012	26 Jan 2013	14
109251	S2	Anticyclonic	26.51°S, 105.02°E	25 Sep 2012	26 Dec 2012	11
109543	S3	Anticyclonic	26.51°S, 105.02°E	17 Sep 2012	13 Feb 2013	16
5904218	A1	Anticyclonic	26.00°S, 105.00°E	22 Sep 2012	10 Dec 2012	6
5903955	A2	Cyclonic	32.60°S, 109.50°E	3 Sep 2012	27 Dec 2012	17

590

591 Table 2. Selected eddy properties determined from the 2012 shipboard data compared
592 with eddies observed in 2003. Eddy properties for the 2003 eddies are from Feng et al.
593 (2007).

	Anticyclonic eddy		Cyclonic eddy	
	2012	2003	2012	2003
Center longitude	105°E	111°46.10'E	109°29.8'E	109°55.10'E
Center latitude	26°30'S	31°8.10'S	32°36'S	31°0.80'S
Average radius (km)	80	63	50	49
Peak velocity (cm s^{-1})	73	65	40	60
Height amplitude (cm)	46	19	26	21
17.5 °C isotherm D (m)	296	262	110	95
Potential vorticity $(\zeta+f)/D$ (m^{-1} s^{-1})	-2.77×10^{-6}	-2.1×10^{-7}	-5.5×10^{-6}	-1.1×10^{-6}

594

595

596

597 Table 3. Rotation period and the mean and range of loop radius for 3 surface drifters in
598 an anticyclonic eddy, determined by the 3 methods as described in Section 2.2. Loop
599 radius derived from the satellite SLA data is also included for comparison.

Drifters					SLA
Number	Period(day)	Radius (km)			Radius (km)
		Method 1	Method 2	Method 3	Method 4
S1	7.96 (4.25-16.75)	40 (22-69)	22 (9-45)	39 (20-68)	102 (61-136)
S2	7.11 (4.25-10.50)	42 (31-61)	40 (32-46)	44 (23-65)	
S3	6.65 (4.00-15.00)	22 (12-33)	40 (30-46)	19 (8-31)	

600

601 **Figure captions**

602 Figure 1. Voyage tracks in 2012 with thirty-minute averaged shipboard ADCP
603 velocities, averaged over the top 200m (vectors). CTD station positions (with station
604 numbers) and trajectories of the 2 bio-optical Argo floats, and 3 surface drifters are
605 shown. Dates are marked along the trajectories at 1 month intervals.

606 Figure 2. Vertical sections crossing the anticyclonic eddy along 105°E (left panels) and
607 crossing the cyclonic eddy (right panels). Potential temperature (a, d), practical salinity,
608 PSS-78 (b, e) and ADCP velocity normal to the sections: eastward velocity (c) and
609 northward velocity (f).

610 Figure 3: Temperature-salinity profiles from the CTD stations at the centre of the
611 anticyclonic eddy (105.0027°E, 26.4982°S) and cyclonic eddy (109.4986°E,
612 32.6201°S), and those from September World Ocean Atlas climatology at the formation
613 location of the eddies, that is, 104.75°E-105.25°E, 26.25°S-26.75°S and 109.75°E-
614 109.25°E, 32.25°S-32.75°S; the LC-WOA was from the area 113°E-115°E, 29°S-31°S
615 in July 2012.

616 Figure 4: Monthly Argo float and drifter tracks in the anticyclonic eddy with monthly
617 sea level anomalies (a-f), sea surface temperature anomalies (g-l), and surface
618 chlorophyll concentrations (log-scale, m-r) during September 2012 to February 2013.

619 Figure 5. Sea surface height anomaly fields prior to the voyage in the southeast Indian
620 Ocean on 28 May (a), 28 June (b), 28 July (c) and 28 August (d) of 2012. The dashed
621 square follows the anticyclonic eddy in each panel, and the solid square follows the
622 cyclonic eddy. The cyclonic eddy could not be identified in May and June. The solid
623 lines denote the center locations of the cyclonic during its evolution.

624 Figure 6. Examples of loops detected using data from three drifters (a, b, c) and one
625 Argo (d). The bold lines denote closed loops of drifter trajectories that are used to derive
626 the eddy properties. The mean eddy drifting velocities are calculated from the

627 translation of the eddy centers derived from the closed loops of drifter trajectories. The
628 WMO ID numbers of the drifters are labeled at the bottom left corner of each panel.

629 Figure 7. SLA map and Argo track (red line) from September 1st to December 21st. The
630 magenta portion of the Argo track identifies the positions recorded on the day of the
631 SLA image.

632 Figure 8. The relationship between tangential velocity of the anticyclonic eddy and
633 distance from the eddy center. The gray dots are derived from the ADCP data at 29m
634 level, fitted with a second order polynomial curve (black line). Colored dots are from
635 6-hourly drifter data. Blue, red and green lines are linear fits to the data points for the
636 three drifters in the range of 0 to 60km from the eddy center.

637 Figure 9. Drifter position relative to the anticyclonic eddy center as calculated by
638 subtracting the mean eddy position from the 6-hourly drifter positions (top); time-series
639 of distance between the drifter position and eddy center (middle); the power spectrum
640 of distance between the drifter position and eddy center (bottom). In the top panels, the
641 black triangle means the start and the black square means the end of the trajectory. In
642 the lower panels, the black lines are the red noise power spectrum of the distance to
643 eddy centre, averaged over 100 realizations.

644 Figure 10. (a) Time series of distance to the anticyclonic eddy center for the Argo float
645 (red curve) and mixed layer depth (blue curve) observed by Argo float A1 (ID:
646 5903955), and (b) evolution of upper ocean potential density measured from the Argo
647 float. The mixed layer depth is defined as the depth where the density is 0.125 higher
648 than that at 10 m depth. The red line in (b) highlights the 25.5 potential density contour.

649 Figure 11.Time series of distance from anticyclonic eddy center (a), the relationship
650 between standardized radial distance and local Rossby number during time period T1
651 (b), T2 (c), and T3 (d). Black dashed line in (a) is the eddy radius from SLA data and
652 the color lines show the distance of the three drifters. T1, T2, and T3 are three

653 representative one-day time periods. T1 is 30 Sep. 2012, T2 is 10 Oct. 2012, and T3 is
654 20 Oct. 2012. The local Rossby number values in (b), (c), and (d) of the drifters are
655 calculated from local velocity gradients at the drifter locations. Solid lines are linearly
656 fits to the data points.

657

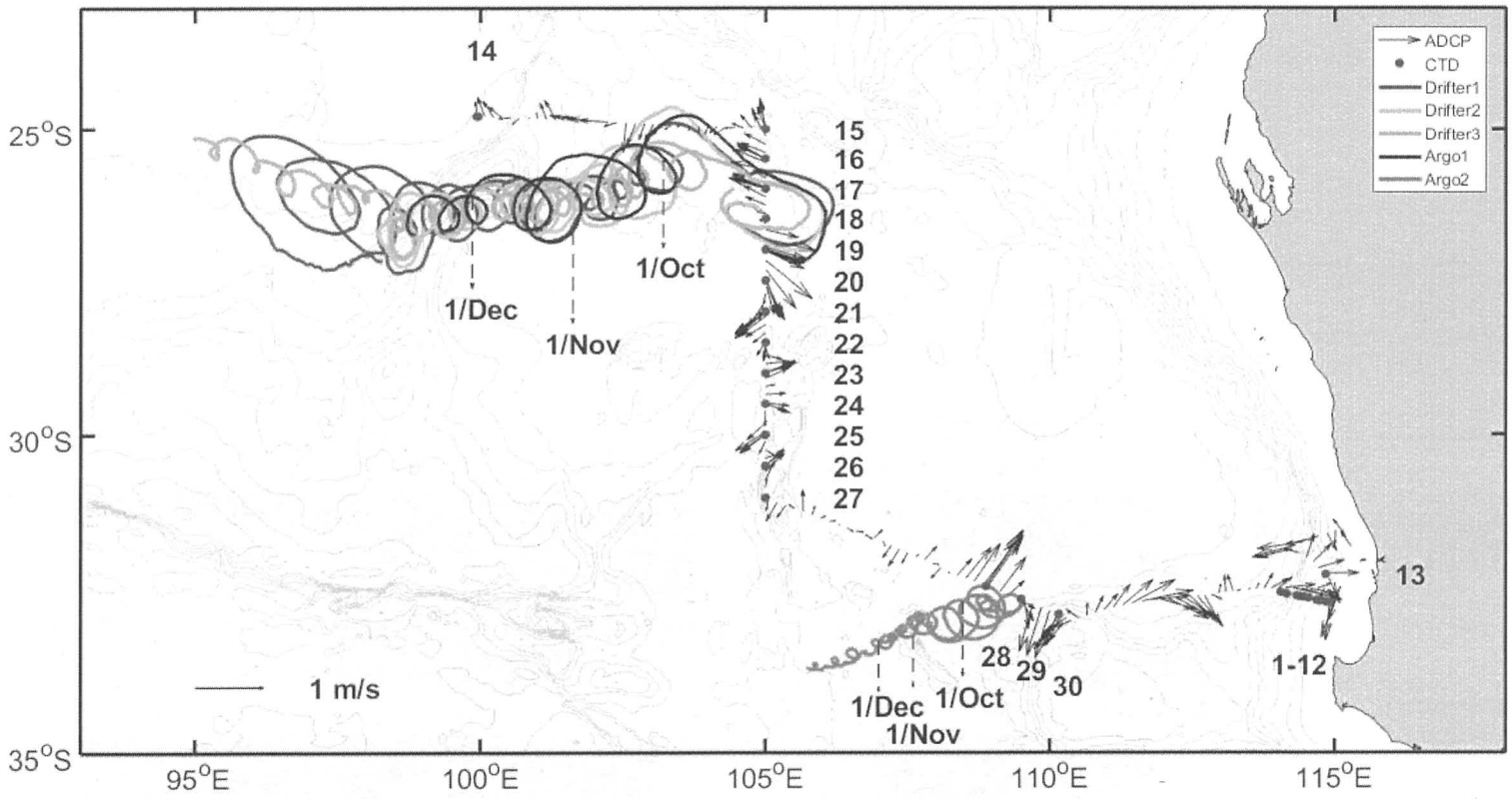
ADCP
CTD
Drifter1
Drifter2
Drifter3
Argo1
Argo2
14
15
16
17
18
19
20
21
22
23
24
25
26
27
1/Oct
1/Dec
1/Nov
13
1-12
28
29
30
1/Dec
1/Nov
1/Oct
1 m/s
25°S
30°S
35°S
95°E
100°E
105°E
110°E
115°E

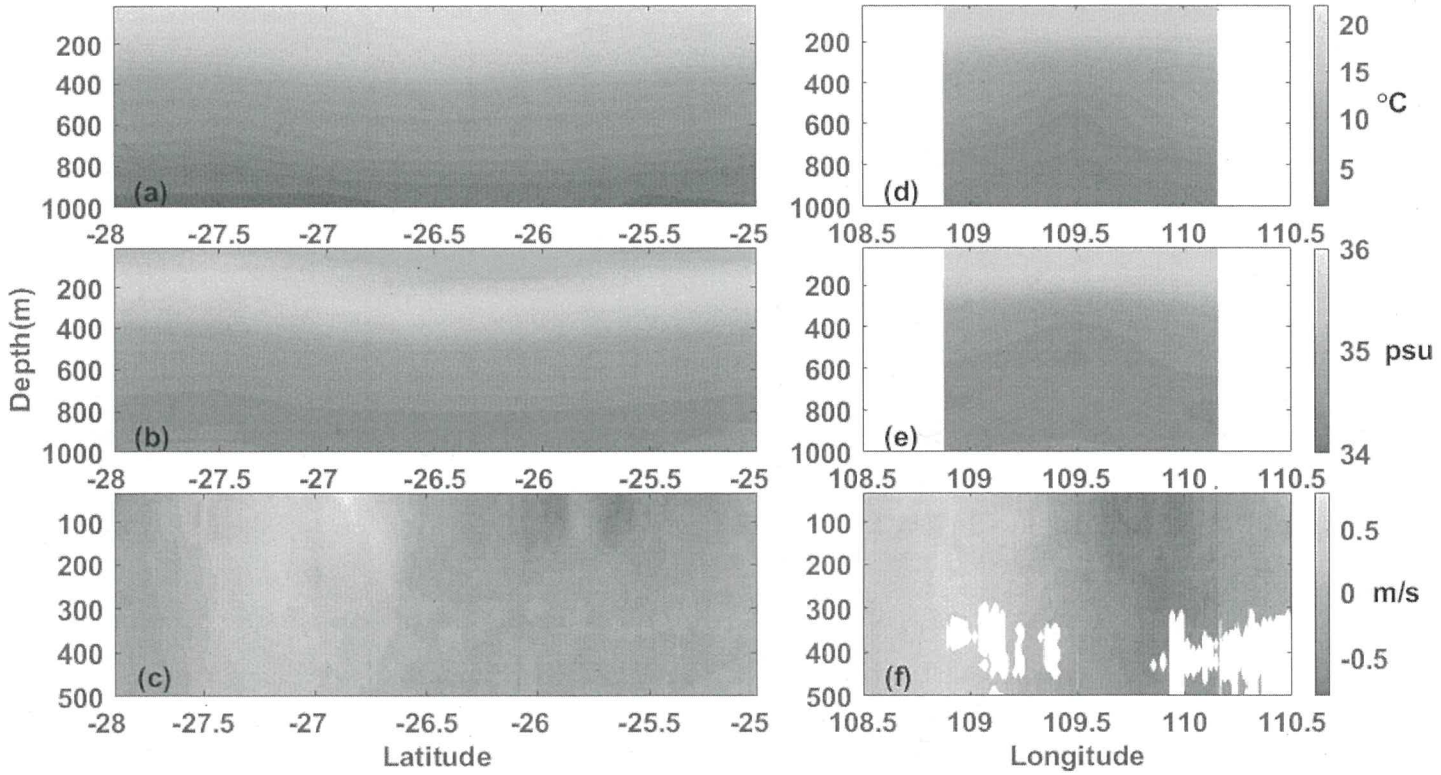
(a)
(b)
(c)
(d)
(e)
(f)
Depth(m)
Latitude
Longitude
°C
psu
m/s
200
400
600
800
1000
100
300
500
-28
-27.5
-27
-26.5
-26
-25.5
-25
108.5
109
109.5
110
110.5
20
15
10
5
36
35
34
0.5
0
-0.5

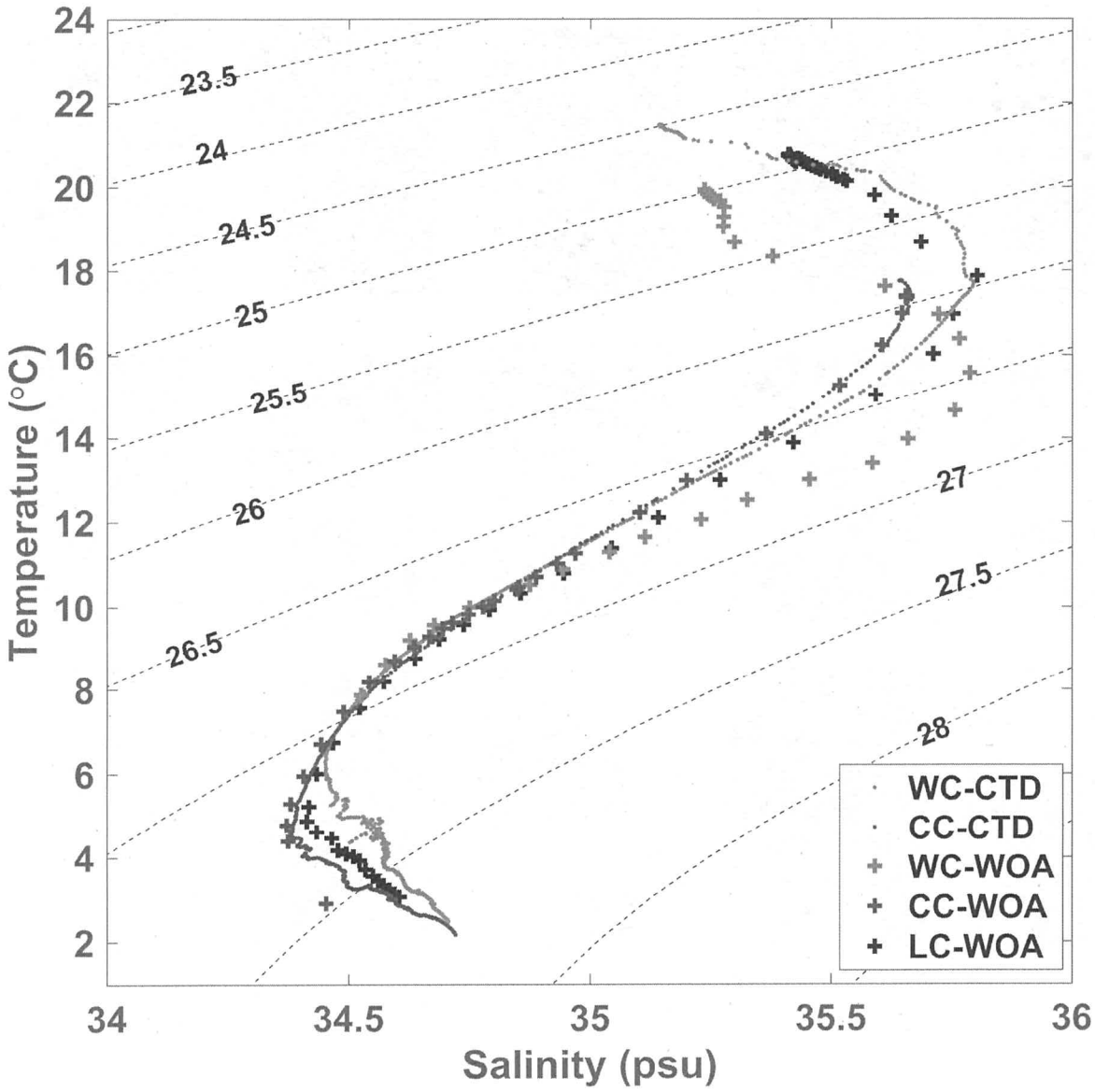
Temperature (°C)
Salinity (psu)
24
22
20
18
16
14
12
10
8
6
4
2
34
34.5
35
35.5
36
23.5
24
24.5
25
25.5
26
26.5
27
27.5
28
WC-CTD
CC-CTD
WC-WOA
CC-WOA
LC-WOA

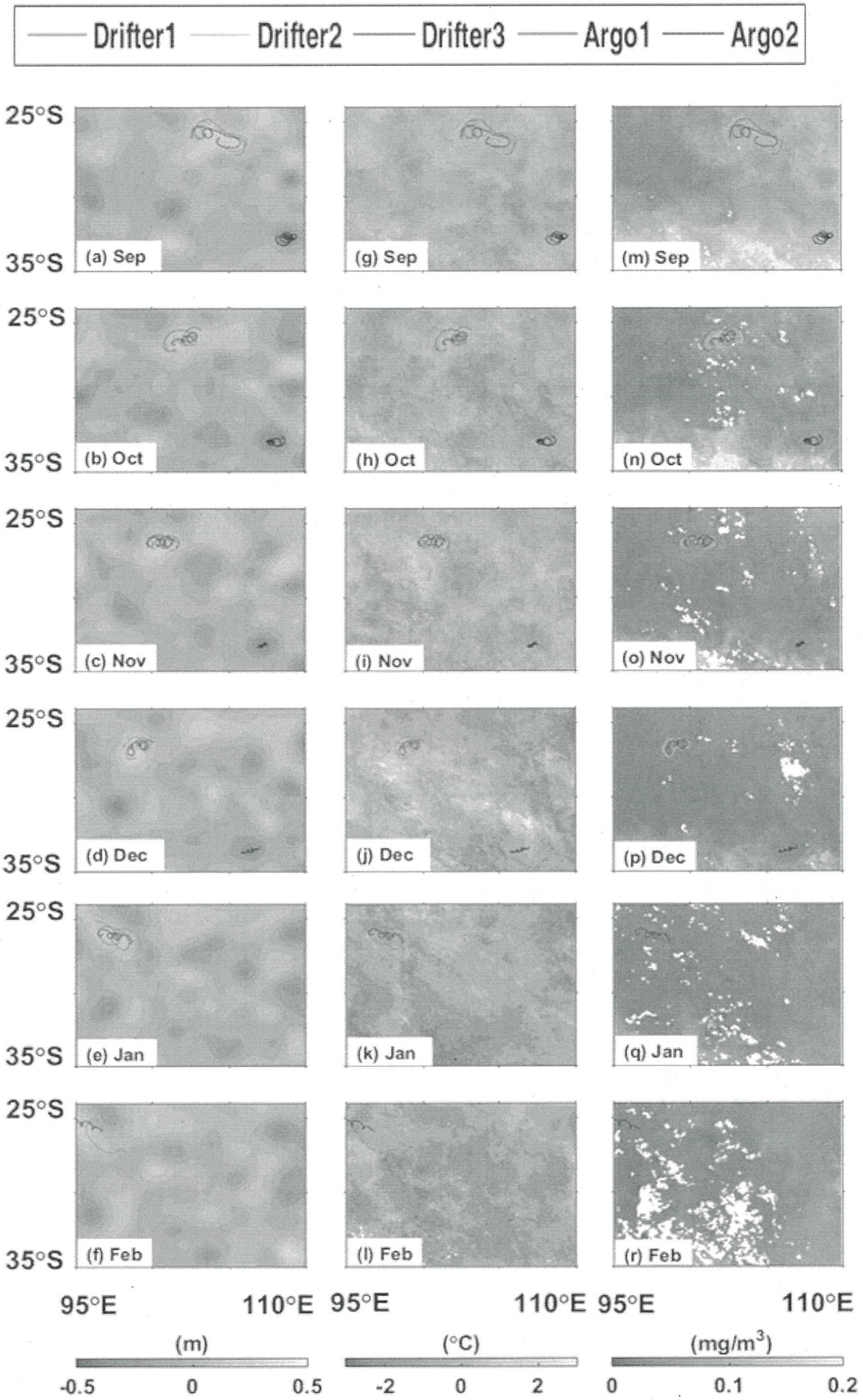
Drifter1
Drifter2
Drifter3
Argo1
Argo2
25°S
35°S
(a) Sep
(g) Sep
(m) Sep
(b) Oct
(h) Oct
(n) Oct
(c) Nov
(i) Nov
(o) Nov
(d) Dec
(j) Dec
(p) Dec
(e) Jan
(k) Jan
(q) Jan
(f) Feb
(l) Feb
(r) Feb
95°E
110°E
(m)
-0.5
0
0.5
(°C)
-2
0
2
(mg/m3)
0
0.1
0.2

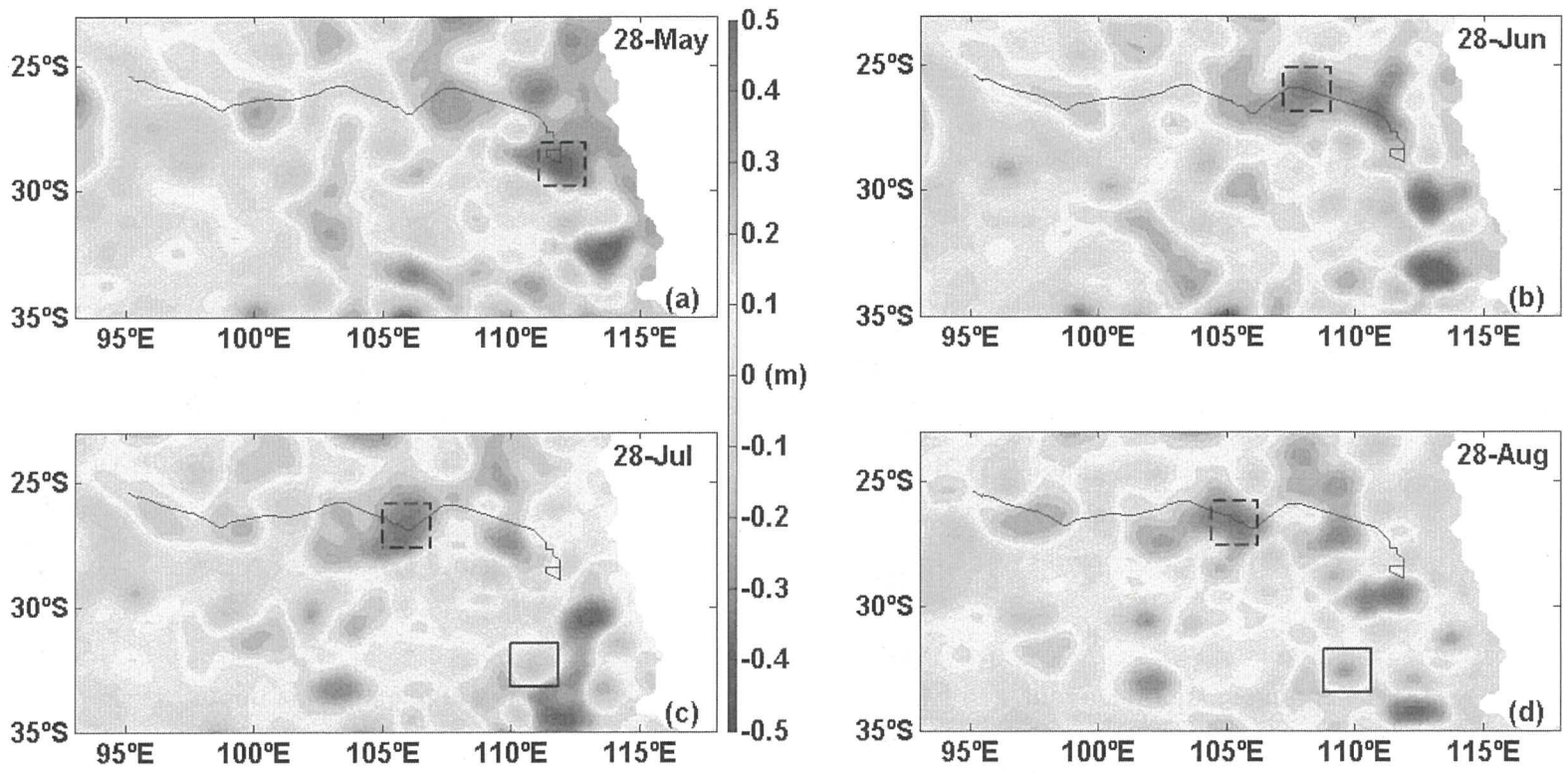
28-May
28-Jun
28-Jul
28-Aug
(a)
(b)
(c)
(d)
25°S
30°S
35°S
95°E
100°E
105°E
110°E
115°E
0.5
0.4
0.3
0.2
0.1
0 (m)
-0.1
-0.2
-0.3
-0.4
-0.5

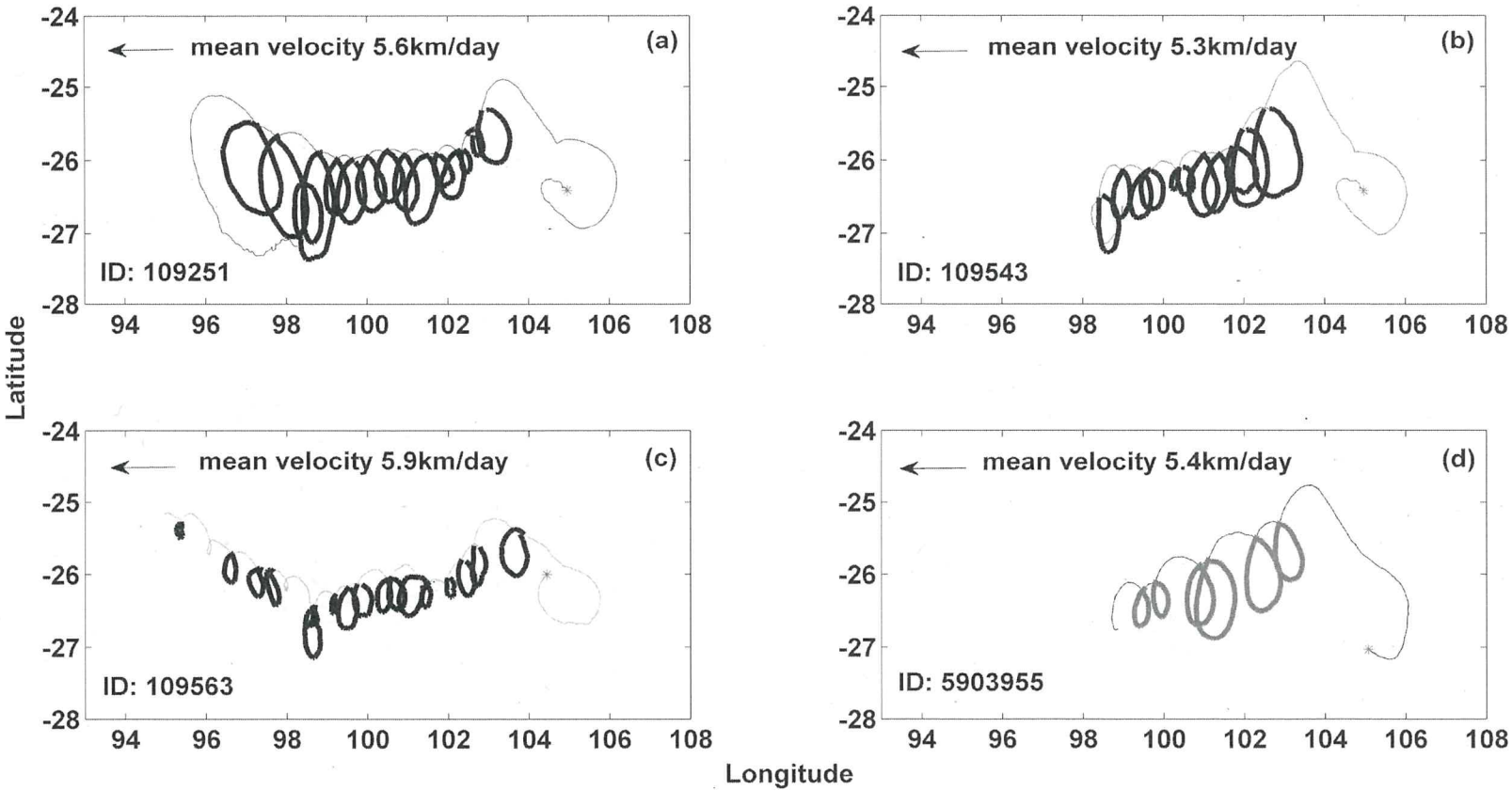
mean velocity 5.6km/day
(a)
ID: 109251
mean velocity 5.3km/day
(b)
ID: 109543
mean velocity 5.9km/day
(c)
ID: 109563
mean velocity 5.4km/day
(d)
ID: 5903955
-24
-25
-26
-27
-28
94
96
98
100
102
104
106
108
Latitude
Longitude

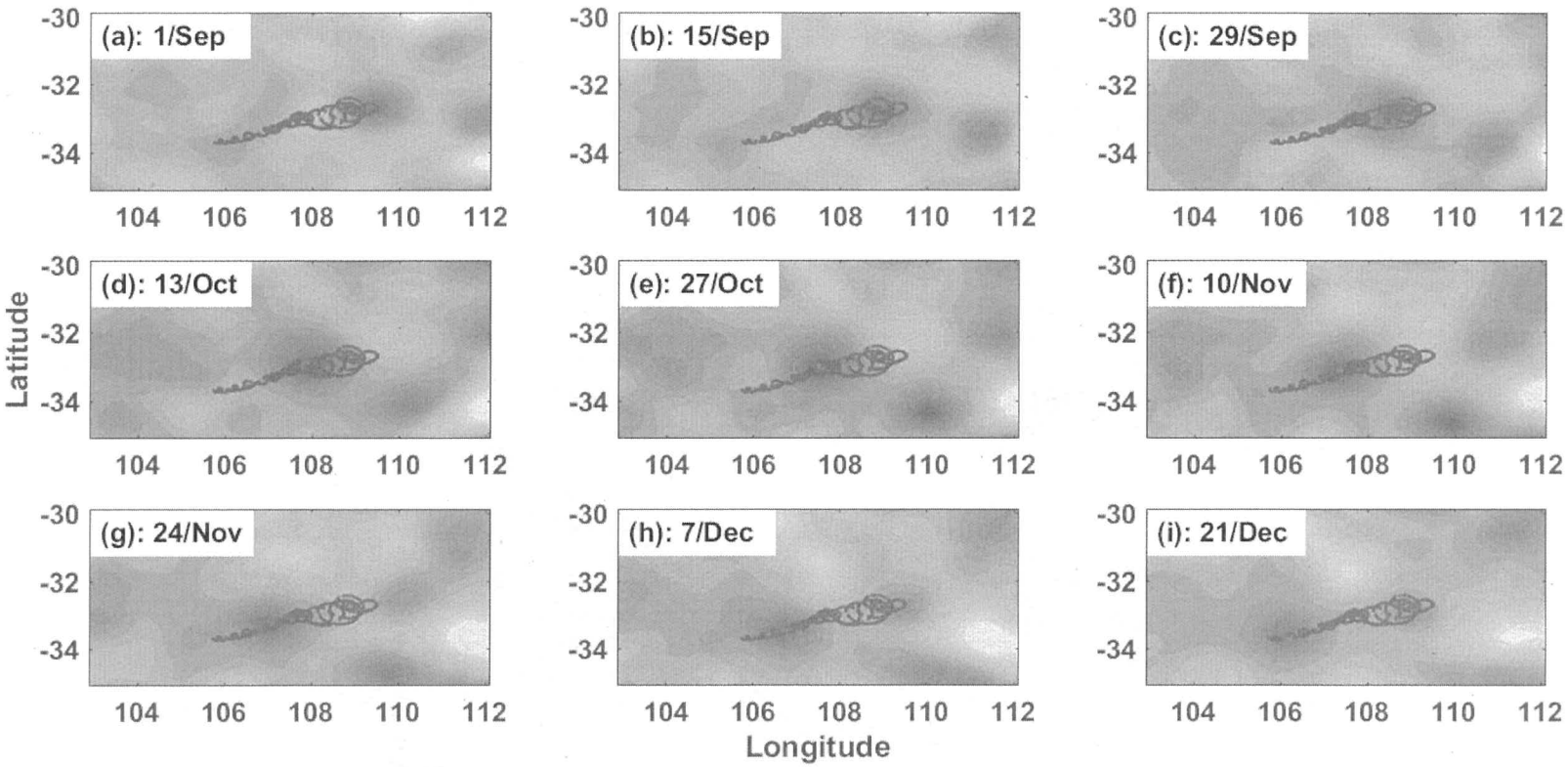
(a): 1/Sep
(b): 15/Sep
(c): 29/Sep
(d): 13/Oct
(e): 27/Oct
(f): 10/Nov
(g): 24/Nov
(h): 7/Dec
(i): 21/Dec
-30
-32
-34
104
106
108
110
112
Latitude
Longitude

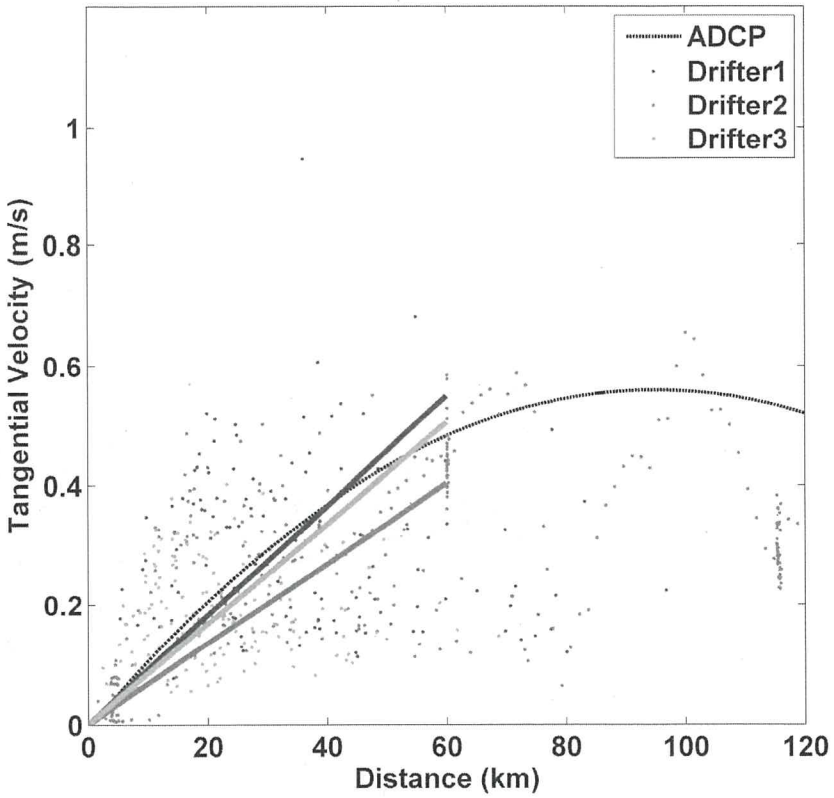
ADCP
Drifter1
Drifter2
Drifter3
Tangential Velocity (m/s)
0
0.2
0.4
0.6
0.8
1
0
20
40
60
80
100
120
Distance (km)

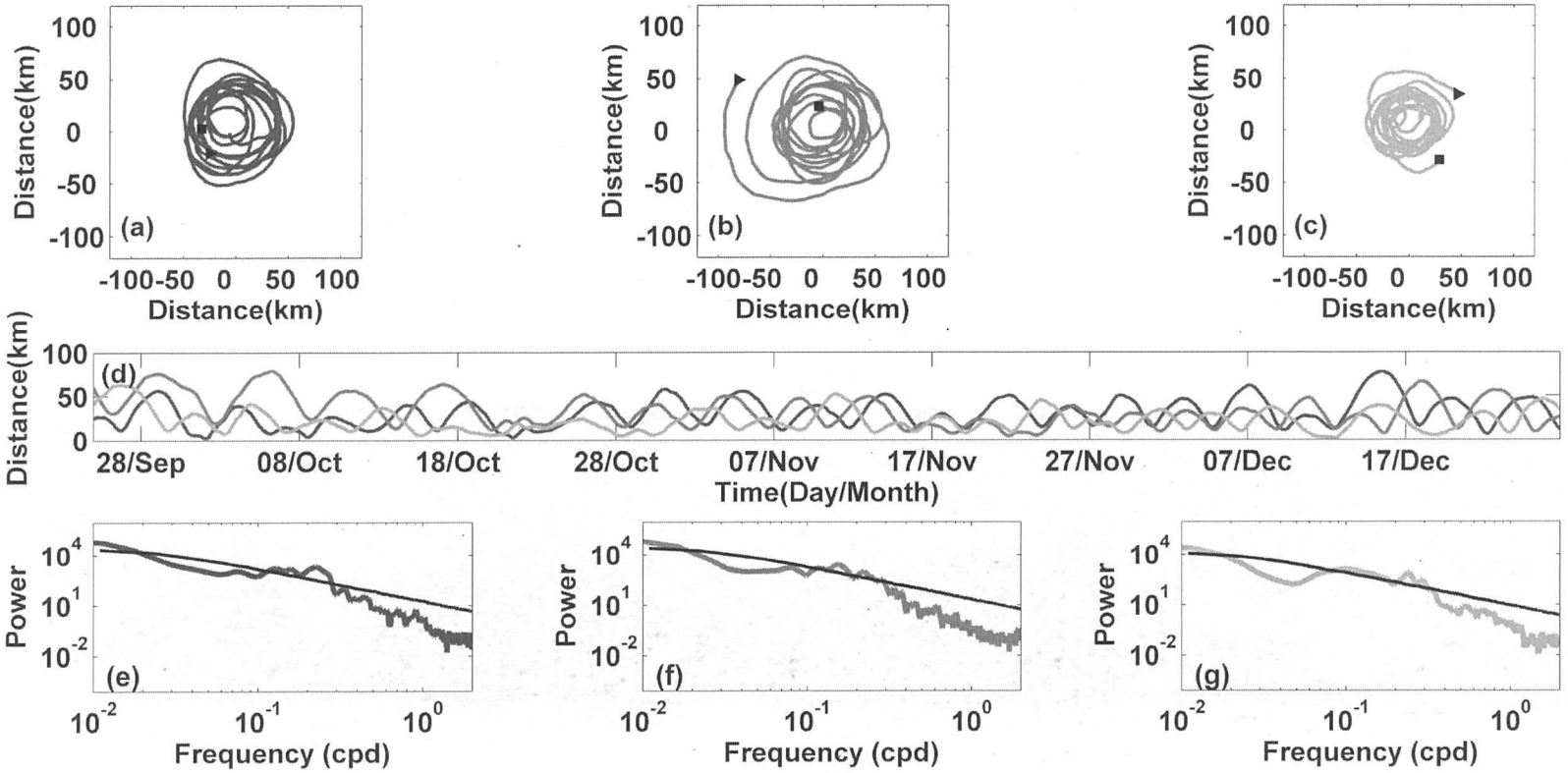
(a)
(b)
(c)
(d)
(e)
(f)
(g)
Distance(km)
100
50
0
-50
-100
-100-50 0 50 100
Distance(km)
28/Sep
08/Oct
18/Oct
28/Oct
07/Nov
17/Nov
27/Nov
07/Dec
17/Dec
Time(Day/Month)
Power
10^{4}
10^{1}
10^{-2}
10^{-2}
10^{-1}
10^{0}
Frequency (cpd)

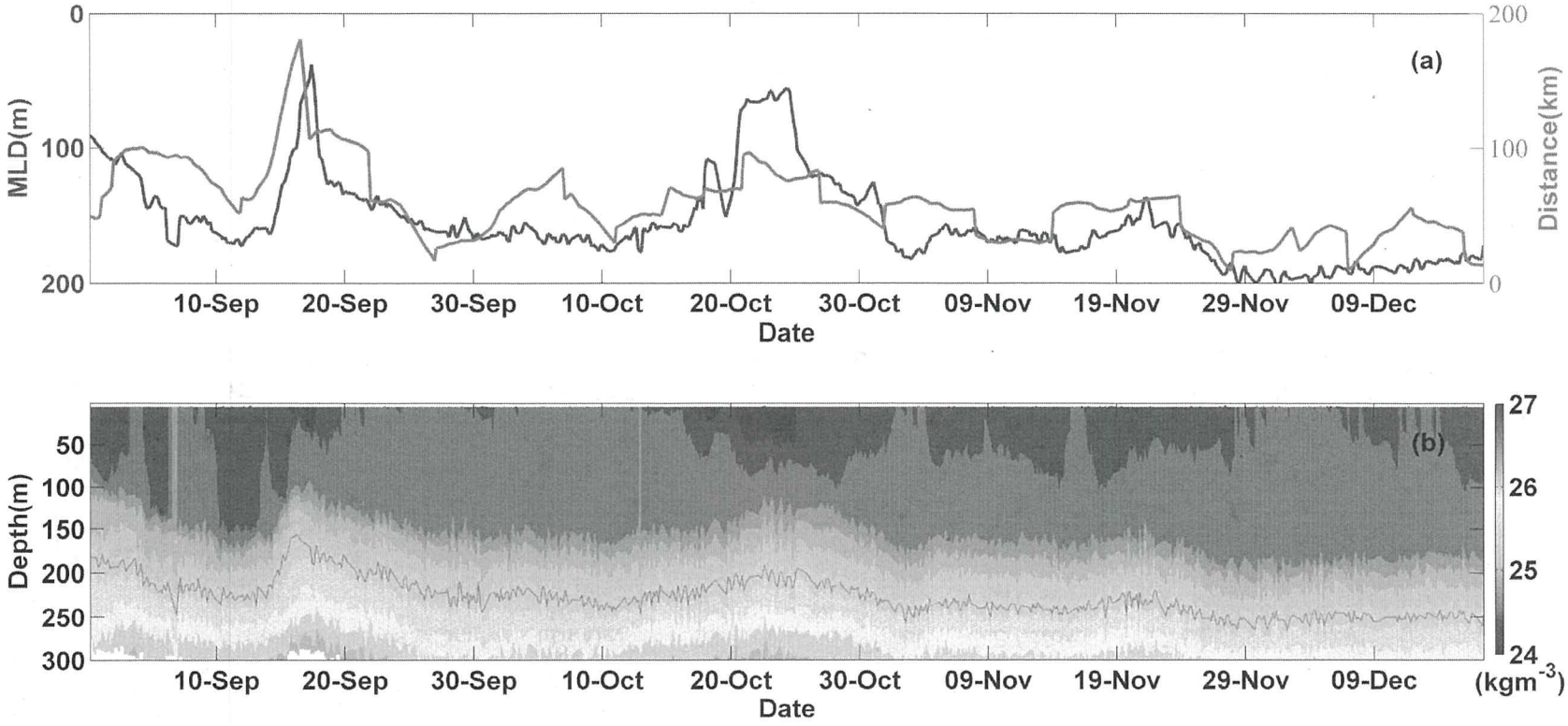
0
100
200
MLD(m)
200
100
0
Distance(km)
(a)
10-Sep
20-Sep
30-Sep
10-Oct
20-Oct
30-Oct
09-Nov
19-Nov
29-Nov
09-Dec
Date
50
100
150
200
250
300
Depth(m)
(b)
27
26
25
24
(kgm-3)
10-Sep
20-Sep
30-Sep
10-Oct
20-Oct
30-Oct
09-Nov
19-Nov
29-Nov
09-Dec
Date

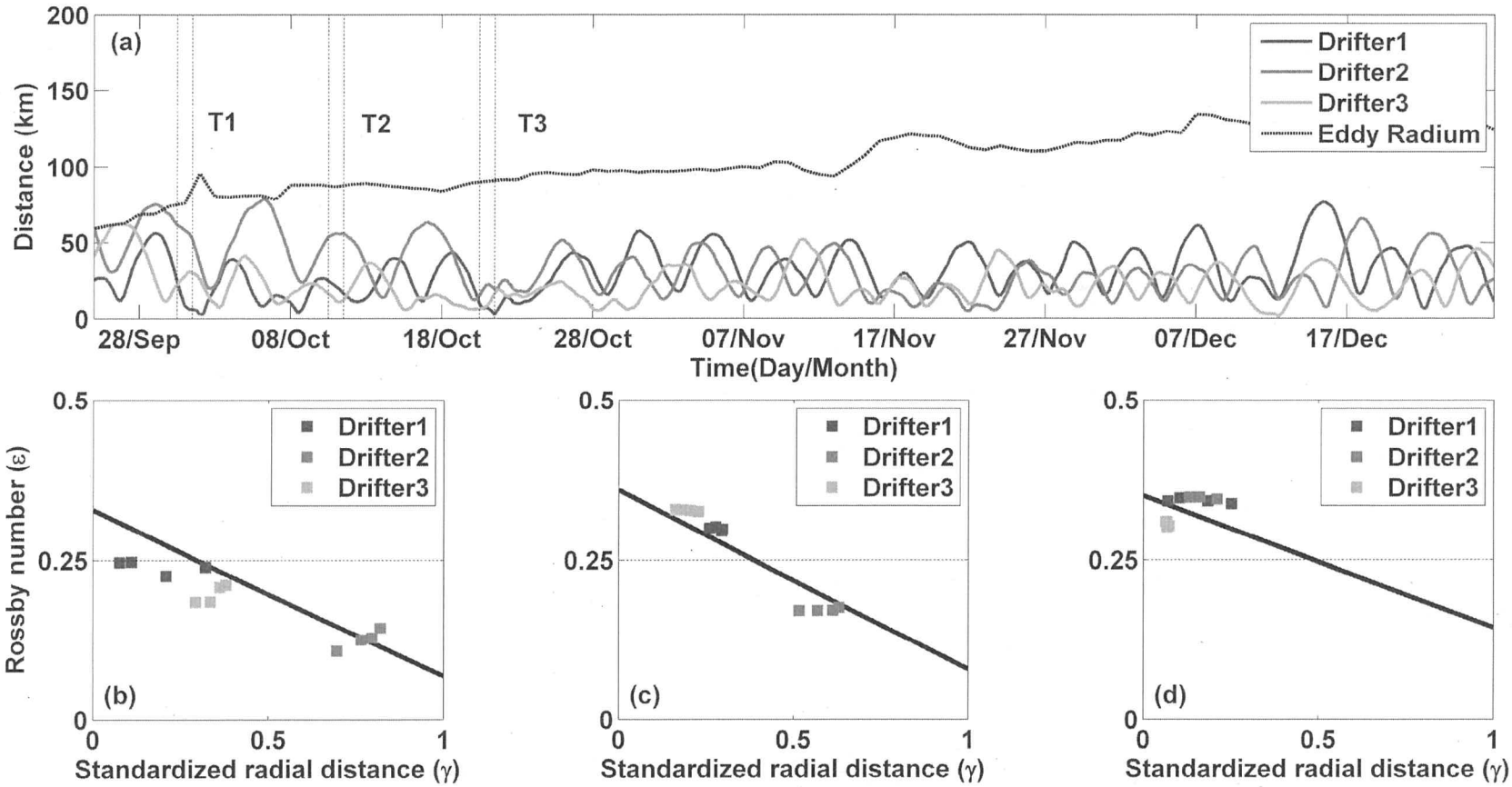
(a)
T1
T2
T3
Drifter1
Drifter2
Drifter3
Eddy Radium
Distance (km)
200
150
100
50
0
28/Sep
08/Oct
18/Oct
28/Oct
07/Nov
17/Nov
27/Nov
07/Dec
17/Dec
Time(Day/Month)
(b)
(c)
(d)
Rossby number (ε)
0.5
0.25
0
0.5
1
Standardized radial distance (γ)